

Assessment of Electrochemical and Mechanical Behavior of Hot-Extruded Powders and As-Cast Samples of Al-Ni Alloys

Wislei R. Osório^{1, 2}, Emmanuelle S Freitas², José E. Spinelli^{3,*}, Manuel V. Canté²,
Conrado R.M. Afonso³, Amauri Garcia²

¹ School of Applied Sciences / FCA, University of Campinas, UNICAMP, Campus Limeira, 1300, Pedro Zaccaria St., Jd. Sta Luiza, 13484-350 Limeira, SP, Brazil

² Department of Materials Engineering, University of Campinas, UNICAMP, P.O. Box 6122, 13083 – 970 Campinas, SP, Brazil

³ Department of Materials Engineering, Federal University of São Carlos, UFSCar, 13565-905 São Carlos, SP, Brazil

*E-mail: spinelli@ufscar.br

Received: 28 July 2012 / Accepted: 4 September 2012 / Published: 1 October 2012

The cellular or dendritic morphologies of the Al-rich matrix as well as the morphology, size, and distribution of the intermetallic particles can affect not only the electrochemical corrosion resistance but also the mechanical strength of Al-Ni alloys. The aim of this work is to analyze the effects of two different powder size (d) ranges ($d < 45 \mu\text{m}$; $106 \mu\text{m} < d < 180 \mu\text{m}$) of Al-Ni alloy samples prepared by nitrogen gas atomization followed by compaction and hot extrusion consolidation, on the microstructure, corrosion behavior and mechanical properties. The corresponding characteristics and properties of directionally solidified Al-Ni alloy samples (as cast) are also examined. Electrochemical impedance spectroscopy (EIS), potentiodynamic polarization techniques and an equivalent circuit analysis were used to evaluate the electrochemical behavior in a 0.5 M NaCl solution at room temperature. It was found that finer microstructure arrays are associated with better electrochemical behavior. This was shown to be intimately associated with fragmented or globular Al_3Ni intermetallic particles, which detached from the eutectic mixture reducing the cathode area and interfering in the corrosion action. A combined plot of corrosion and mechanical properties as a function of a representative microstructural parameter is proposed, permitting an appropriate combination of these properties to be designed based on the alloy microstructure.

Keywords: Al-Ni alloy; Hot Extrusion; Gas atomization; Microstructure; Mechanical properties; Corrosion resistance

1. INTRODUCTION

The eutectic Al-6%Ni alloy has been extensively investigated mainly due to its attractive microstructure, which encompasses the ductility of the aluminum matrix and hard particles of the Al₃Ni phase [1]. The development of optimized structures on such alloys may depend on the solidification process even when some post-processing is performed. A logical strategy to increase strength without losing plasticity of these alloys seems to be alloying Al-Ni with transition metals such as scandium and zirconium. However, it is important to take into account the additional cost involving the addition of zirconium and especially that of scandium.

Hypoeutectic as-cast Al-Ni alloys are characterized by microstructures composed by a dendritic matrix rich in aluminum surrounded by a eutectic mixture ($\alpha+\beta$), where α is the Al-rich phase and β is the Al₃Ni intermetallics. In this case, the association of a refined structure with a considerable fraction of Al-Ni intermetallics may result in high hardness and, as a consequence, in high mechanical strength [2]. Automotive parts such as connecting rods, cylinder sleeves, pistons and valve retainers as well as compressor parts such as rotary compressor vanes and shoe discs may be manufactured with Al-Ni alloys [3].

Commercial materials with low porosity and appreciable high strength can be prepared by extrusion after being processed by rapid solidification. Aluminum alloy powders can be usually consolidated by extrusion until the full density be reached. One of the routes indicated to obtain very refined intermetallics in metallic alloys is the spray forming process. Spray forming involves an inert gas atomization of a liquid metal stream into variously sized droplets which are then propelled away from the region of atomization by the fast flowing of the atomizing gas [4-5]. The powder which was not incorporated into the deposit and was collected at the bottom of the atomization chamber is called overspray powder and is usually in the range of 20% in weight of the starting charge. The desired microstructural arrangement at this stage is mainly affected by alloy composition and powder size. At this point, the kinetics of solidification can significantly influence the final powder structure. Furthermore, Al alloy atomizing powders form usually supersaturated solid solutions as a consequence of the extremely high cooling rates that are applied during the atomization process. In a recent study [6], a Ni content of 1.5 at.% Ni (~3.0 wt.%) within the α -Al matrix has been reported, induced by rapid quenching during atomization of a hypoeutectic Al-5 wt.% Ni alloy. The solid solubility of Ni in Al is very limited under equilibrium conditions, with a value of 0.023 at.% Ni (~0.05 wt. %). A subsequent annealing may start a decomposition of the supersaturated solid solution.

The dependences of ultimate and yield tensile strengths and elongation on the primary and secondary dendritic arm spacings have already been reported for hypoeutectic Al-Ni alloys [7]. Both the scale of the dendritic microstructure and the solute content affect the plastic tensile properties of Al-Ni alloys. Smaller dendritic spacings allow a better distribution of the hard Al₃Ni intermetallic phase reinforcing the ductile Al-rich phase of the eutectic mixture located in the interdendritic regions. This leads to improvements in the mechanical strength. It is well known that the control of the microstructure has an important role on a number of properties, e.g. mechanical properties and corrosion resistance [8-10].

Osório et al. [10] have recently reported that N₂ gas pressure of 8 bar during spray forming process of an Al-5.0wt%Ni alloy resulted in a microstructure characterized by a high fraction of small powders and fine cell spacings, having improved pitting potential but higher corrosion current density when compared with the corresponding results of a coarser microstructure obtained under lower pressure.

Very few reports are available in the literature regarding the study of rapidly solidified binary Al-Ni alloys and their properties in the range of hypoeutectic chemistries, i.e., a lower solute content than Al-Ni eutectic composition. There is also a lack of experimental investigations concerning the effects of atomizing Al-Ni powder size on joined structures (either by cold or by hot forming) as well as the final microstructure features, mechanical properties and corrosion resistance. Sivtsova et al. [11] compared the microstructure and properties of melt-quenched foils of binary and ternary Al-Ni-(Cr) alloys. The surface of the melt-quenched foils of a dilute Al-0.6 at % Ni was shown to have a cellular structure after being obtained by melt spinning at a cooling rate of about 10⁶ K/s. This alloy exhibits a decrease in the microhardness as the annealing temperature increases. It was also observed that annealing in the temperature range 260-380°C causes additional precipitation of Al₃Ni fine particles from the supersaturated solid solution. Wada et al. [12] examined the strength of hypoeutectic Al-Ni alloys for aluminum-stabilized superconductors. The Al-2.0wt%Ni alloy achieved a yield stress of 120MPa after precipitation heat treatment at 430°C.

Uan et al. [13] carried out hot extrusion (200-400°C) of directionally solidified eutectic Al-Ni samples with an extrusion ratio of 36:1 and ram speed of 40 cm min⁻¹. The final subgrains were reported to be roughly equiaxed, having sizes of 1.14 ± 0.23 μm and 1.56 ± 0.30 μm for billets extruded at 200°C and at 400°C, respectively. The Al₃Ni intermetallics were rod-like shaped for both conditions, being fully distributed intergranularly in the 200°C extruded billet and distributed partially intergranularly and intragranularly in the case of the 400°C extruded billet. The 200°C extruded specimen exhibited a yield stress of 156 MPa at room temperature, which is higher than the corresponding value of 118 MPa for the 400°C extruded specimen.

The effects of powder size on the extrusion behavior of the Al_{88.7}Ni_{7.9}Mm_{3.4} alloy, prepared by nitrogen gas atomization followed by compaction/degassing and hot extrusion, were investigated by Hong and Chun [14]. The hot extrusion was performed with an area reduction ratio of 25:1 at 400°C. Ram speed was kept at 5 mm s⁻¹. The different powder particles showed different hardness (the hardness increased with the decrease in particle size). The powder particles with diameter less than 26 μm consisted of nanocrystalline particles of aluminum embedded in an amorphous matrix.

Jorge Jr et al. [15] investigated the effect of process parameters on the microstructure and mechanical properties of nanostructured powders of Al-3Fe and Al-4.5Cu alloys consolidated by hot extrusion. The proper use of the process parameters such as the extrusion temperature and strain rate associated with the presence of fine precipitates were determinants in the control of grain growth during the hot consolidation improving the mechanical properties with compressive stress of about 400 MPa.

In view of the number of alternative practices which has been proposed nowadays to improve both corrosion behavior and mechanical properties of promising structural Al-alloys such as Al-Ni alloys, the present study aims to establish a correlation between the microstructure features found in a

hot-extruded Al-3 wt.% Ni powder alloy (prepared by gas nitrogen atomization followed by compaction and hot extrusion) and the corresponding electrochemical corrosion resistance and mechanical properties. Temperature, ram speed and extrusion ratio were maintained constant for the two different ranges of powder size. The work deals further with a direct comparison of the results obtained with powder hot extruded and directionally solidified samples of an Al-3 wt.% Ni alloy.

2. EXPERIMENTAL PROCEDURE

2.1 Preparation of hot-extruded powder samples

The spray forming process also named spray casting or spray deposition is based on the inert gas atomization of a liquid metal stream into variously sized droplets which are then propelled away from the region of atomization by the fast flowing atomizing gas. A charge weighting about 2.0 (± 0.1) kg of a hypoeutectic Al-3 wt.% Ni alloy was prepared using commercially pure grade (c.p.) Al and Ni [8-9], i.e. Al (99.887 wt.%) and Ni (99.896 wt.%). The mean impurities detected were: Fe (0.059%), Si (0.042%), Sn (0.0073%), Ni (0.0057%) and Pb (0.0027%), besides other elements found with concentrations less than 100 ppm.

The melt was poured via a nozzle of 6 mm diameter fixed at the bottom of a tundish when the melt temperature was about 10% above the *liquidus* temperature (710°C). When the melt was poured, a nitrogen (N₂) flow was simultaneously started under a pressure of 0.8 MPa. The overspray alloy powders were collected at the bottom of the atomization chamber.

Then, the powder was sieved and classified in two particle size ranges: particle size less than 45 μm (range d1); and particle size less than 180 μm and higher than 106 μm (range d2).

Cold compaction (with 600 \pm 5 MPa of uniaxial stress) was used to transform samples of each range of powder size into cylindrical samples with a diameter of 25.0 (\pm 0.2) mm and a weight of about 20.0 (\pm 0.2) g. The cold pressing of the powders were made without canning, degassing, and atmosphere control, and were compacted in air at room temperature (± 25 °C).

The preforms were then consolidated by hot extrusion at 350°C with ram speed of 5 mm.s⁻¹ and extrusion ratio of 5:1, resulting into cylindrical compact products with diameter of 12.7 \pm 0.2 mm. The mechanical properties of the bulk material consolidated from the Al-3 wt.% Ni alloy powders were determined by means of room-temperature (about 25 °C) tensile tests, which were performed according to specifications of ASTM Standard E 8 M using a Instron[®] 5500R machine at a strain rate of 1 \times 10⁻³ s⁻¹ in the elastic range and of 4 \times 10⁻³ s⁻¹ in the plastic range. Three specimens were tested for each selected powder size range in an Instron[®] 5500R machine in order to ensure reproducibility of the tensile tests results.

2.2 Directionally solidified Al-3 wt.% Ni alloy samples

A directionally solidified casting of the Al-3 wt.% Ni alloy is shown in Fig. 1. It was grown in an experimental setup that was designed in such way that heat was extracted only through the water-

cooled bottom, promoting vertical upward directional solidification. Specimens were extracted from longitudinal sections, ground by silicon carbide papers up to 1200 mesh, polished and etched to reveal the microstructure. Continuous temperature measurements in the casting were monitored during solidification via the output of a bank of fine type K thermocouples sheathed in 1.6 mm outside diameter (o.d.) stainless steel tubes, and positioned at different positions from the heat-extracting surface at the bottom of the casting. All thermocouples were connected by coaxial cables to a data logger interfaced with a computer and the temperature data were acquired automatically.

The casting was sectioned along the longitudinal direction and the macrostructure was revealed. Transverse specimens were cut from the casting and prepared for tensile testing. Tensile parameters like yield tensile strength, ultimate tensile strength and elongation have been determined for specimens extracted from different positions in casting with respect to the cooled bottom surface.

2.3 Microstructure characterization

Each sample was electropolished and etched (a solution of 0.5% HF in water) for metallography. After revealing the microstructures, the intercept method was employed to measure both the interphase spacing (λ) and the secondary dendrite arm spacing (λ_2). At least 30 measurements were performed for each selected position along the casting length. An optical microscopy associated with an image processing system Neophot 32 (Carl Zeiss, Esslingen, Germany) and Leica Quantimet 500 MC (Leica Imaging Systems Ltd, Cambridge, England) were used to microstructural characterization.

Microstructural characterization was also performed using a Field Emission Gun (FEG) - Scanning Electron Microscope (SEM) Philips (XL30 FEG). The X-ray diffraction (XRD) patterns have been obtained in a Siemens[®] D5000 diffractometer with a 2-theta range from 20° to 90°, CuK α radiation and a wavelength, λ , of 0.15406 nm. For nano scale characterization, a (Scanning) Transmission Electron Microscope (S)TEM 200kV with a Field Emission Gun (FEG) FEI TECNAI G² F20[®] coupled to an Energy Dispersive Spectroscopy (EDS) detector EDAX SUTW (super ultra-thin window) and a high angle annular dark field (HAADF) detector Fischione[®] Model 3000 was used.

2.4 Electrochemical corrosion tests

The Al-Ni alloy samples were further carefully ground to a 1200 grit SiC finish, followed by distilled water washing and air drying before corrosion tests. Then, the samples were positioned at the glass corrosion cell kit, leaving a circular 1.0 (\pm 0.02) cm² metal surface in contact with a naturally aerated and stagnant 500 cm³ of a 0.5 M NaCl solution at 25°C having a pH of 6.98 (\pm 0.04). EIS measurements began after an initial delay of 15 minutes for the sample to reach a steady-state condition. A potentiostat (EG & G Princeton Applied Research[®], model 273A) coupled to a frequency analyzer system (Solartron[®] model 1250), a glass corrosion cell kit with a platinum counter-electrode and a saturated calomel reference electrode (SCE) were used to perform the EIS tests. The potential

amplitude was set to 10 mV; peak-to-peak (AC signal) in open-circuit, with 5 points per decade and the frequency range was set from 100 mHz to 100 kHz.

Potentiodynamic tests were also carried out in a 0.5 M NaCl solution at 25 ± 3 °C using a potentiostat at the same positions and immediately after the EIS measurements. These tests were conducted by stepping the potential at a scan rate of 0.1667 mVs^{-1} from $-250/+250$ mV (SCE) at open-circuit. Using an automatic data acquisition system, the potentiodynamic polarization curves were plotted and the corrosion rate and potential were estimated by Tafel plots using both anodic and cathodic branches. Duplicate tests for both EIS and potentiodynamic polarization curves were carried out. A model (ZView[®] version 2.1b) for equivalent circuit quantification has also been used in order to supply quantitative support for discussions of EIS measurements.

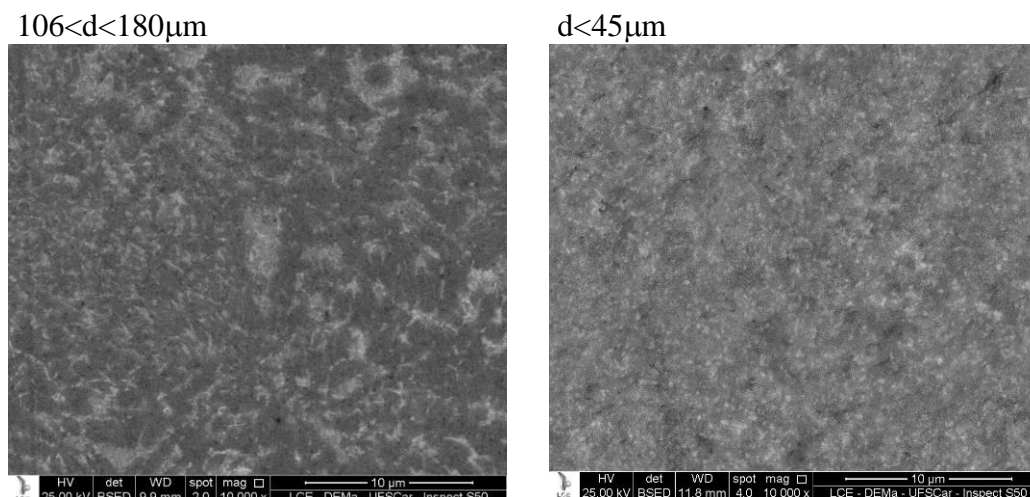
3. RESULTS AND DISCUSSION

3.1 Microstructural characterization of the hot-extruded powder samples

Typical microstructures of two different hot-extruded powder samples can be seen in Fig. 1. The general arrangements are quite different, since the intermetallic particles are better distributed in the hot-extruded (HE) sample having finer powder particles, i.e., an effective intragranular precipitation process seems to have contributed to this condition.

Fig. 2 shows the X-Ray diffractogram (XRD) patterns obtained for the Al-3 wt.% Ni powder alloy as well as for the two hot-extruded samples. The Al_3Ni peaks detected the presence of these intermetallics in the powder and in both hot consolidated samples.

Fig. 3 depicts transmission electron microscopy (TEM) micrographs in different image modes in order to permit microstructure details of hot extruded Al-3 wt.% Ni alloy from coarser powder ($106 < d < 180 \mu\text{m}$) to be characterized. Fig. 3(a) shows a TEM micrograph of bright field (BF) image depicting Al_3Ni intermetallic particles located along the grain boundary (GB) of Al- α grains and corresponding selected area diffraction (SAD) pattern of precipitate which is oriented into $[1\ 1\ 2]_{\text{Al}_3\text{Ni}}$ zone axis.



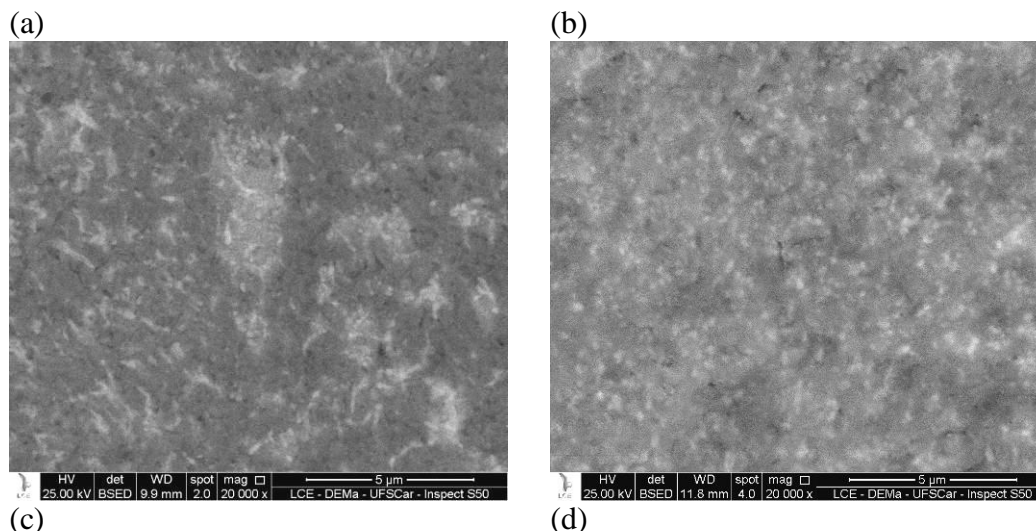


Figure 1. SEM microstructures of hot-extruded Al-3 wt.% Ni alloy samples: (a), (c) coarse ($106 < d < 180 \mu\text{m}$) and (b), (d) fine powders ($d < 45 \mu\text{m}$).

Fig. 3(b) shows a high resolution transmission electron micrograph (HRTEM) of the dashed region of Fig. 3(a), indicating the presence of very fine Al_3Ni precipitates in a nanoscale order of about 3 nm and respective fast Fourier transform (FFT) indicating diffraction spots of $d = 0.36 \text{ nm}$ ($0\ 2\ 0$) $_{\text{Al}_3\text{Ni}}$. Fig 3 (c) and Fig. 3 (d) show high angle annular dark field images in scanning transmission electron microscopy mode (HAADF-STEM) with micrometric Al- α grains and nanometric Al_3Ni particles at the grain boundaries, with some of them barely precipitated within the Al- α grains with ring pattern (bigger selected area aperture) and SAD pattern (smaller selected area aperture) oriented in $[1\ 1\ 1]_{\alpha\text{-Al}}$ zone axis.

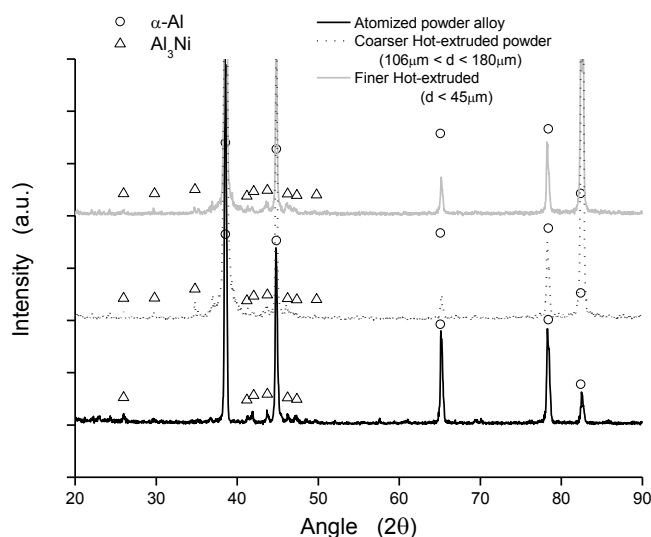


Figure 2. XRD patterns of Al-3 wt.% Ni alloy samples: powder and hot-extruded from powder with the 2 distinct particle sizes.

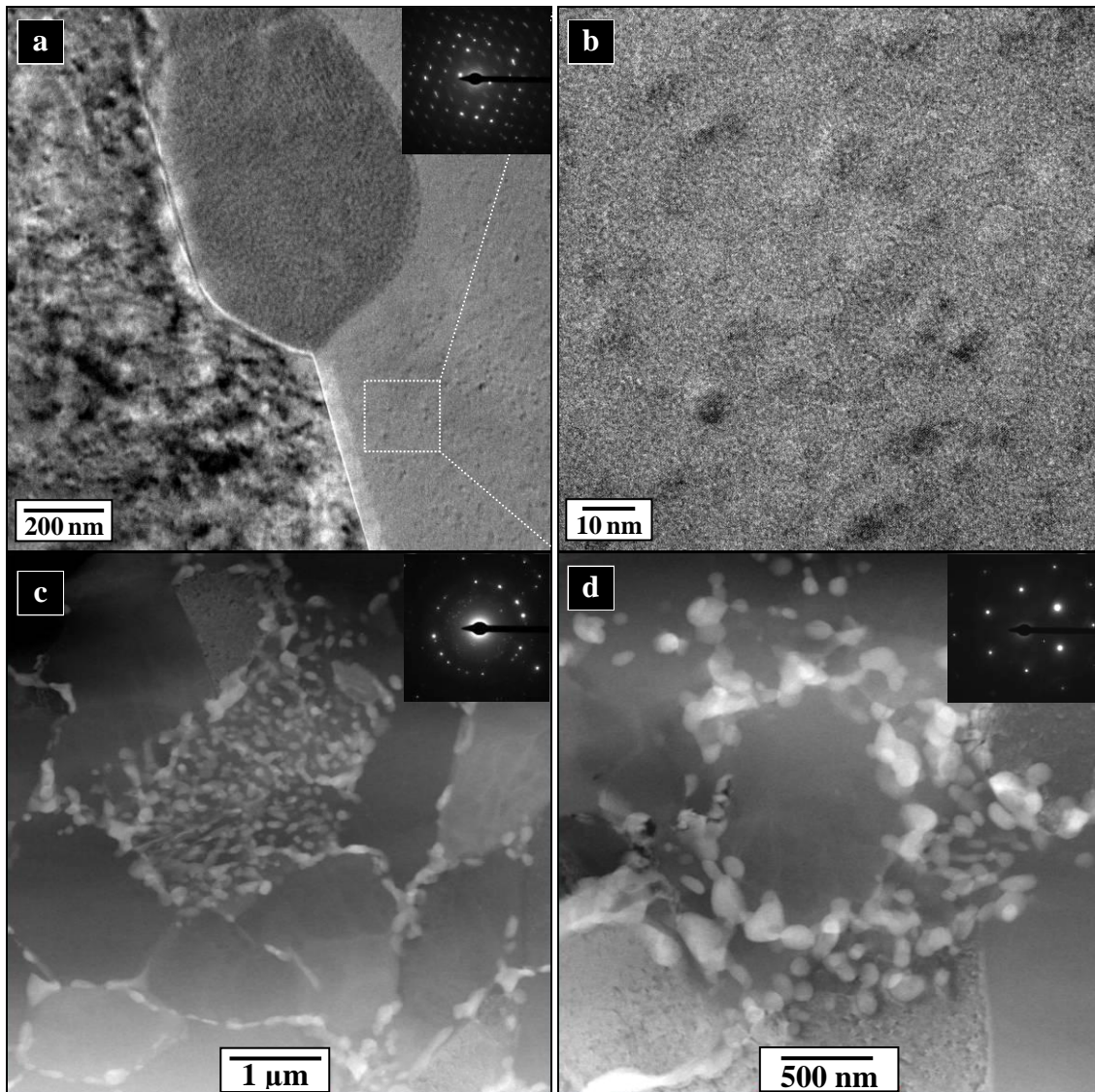


Figure 3. TEM micrographs of the hot-extruded Al-3 wt.% Ni alloy from coarser powder ($106 < d < 180 \mu\text{m}$) showing (a) Al_3Ni particles at the grain boundary (BG) of Al- α grains; (b) high resolution (HRTEM) detail of dashed region in (a); (c) and (d) HAADF-STEM micrograph distribution of nanometric Al_3Ni intermetallic particles with respective SAD patterns.

Fig 4(a) shows a STEM-HAADF micrograph combined with X-ray elemental mapping (Fig. 4(b)) of Ni-K, highlighting the higher concentration of Ni in nanometric particles of Al_3Ni at the grain boundaries and within the Al- α grains.

3.2 Macro and microstructural characterization of the as-cast samples

Fig. 5 shows the macrostructure of the directionally solidified Al-3 wt.% Ni alloy casting, with a prevalence of columnar grains along the casting length. The selected positions from where samples were extracted for corrosion tests are highlighted in Fig. 5(a), i.e. at positions P1 = 10 mm and P2 = 40mm from the bottom of the casting, respectively.

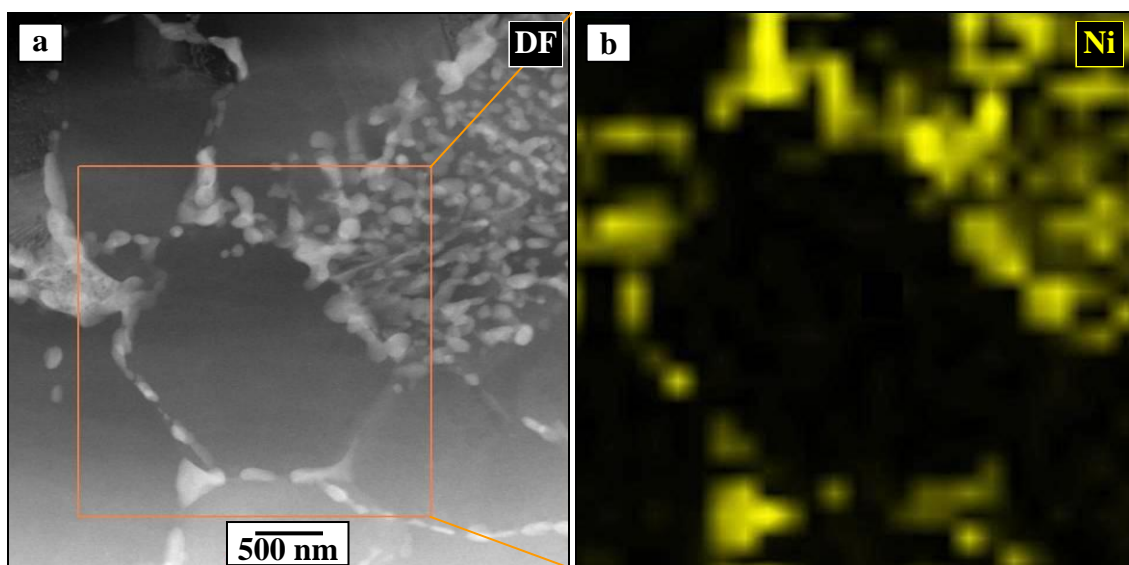


Figure 4. (a) STEM-HAADF micrograph of the hot-extruded Al-3 wt.% Ni alloy sample (powder size from 106 to 180 μm) revealing the particular features of a couple of grains and (b) highlighting the local presence of Ni by X-ray elemental mapping.

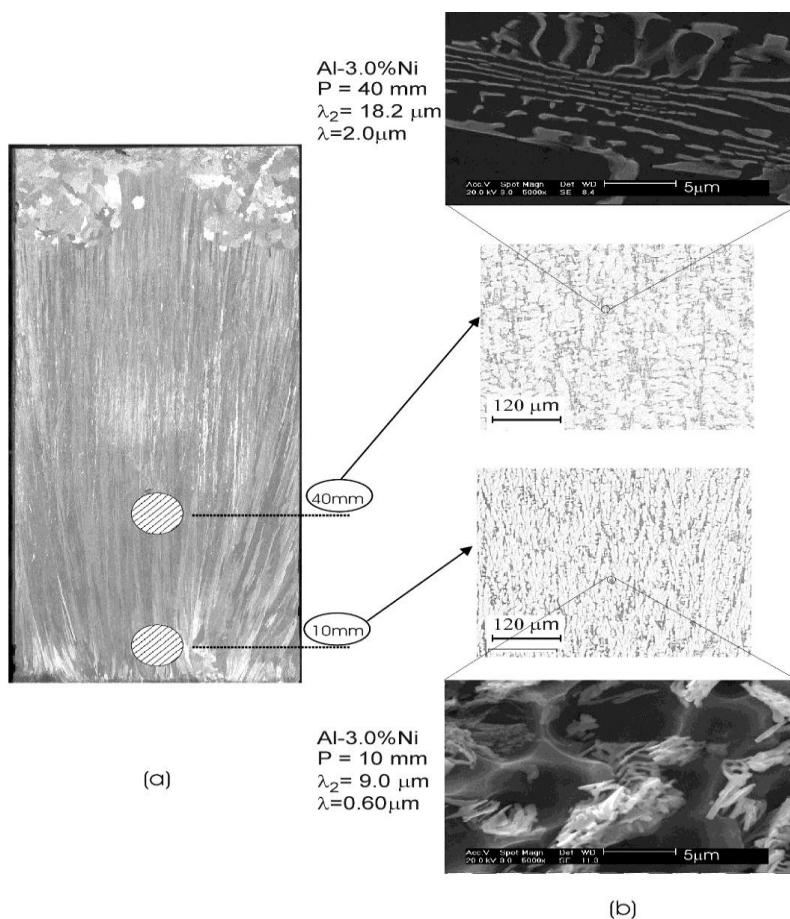


Figure 5. Typical macrostructure of the as-cast Al-3 wt.% Ni alloy and a schematic representation of positions from where the samples were extracted for corrosion tests and (b) optical and SEM micrographs with the corresponding secondary dendritic spacings (λ_2) and interphase spacings (λ).

The final as-cast microstructure is formed by a α -Al dendritic matrix with a eutectic mixture located in the interdendritic regions (Fig. 5(b)). The eutectic phase is composed by the alternation of α -Al and intermetallic Al_3Ni particles. Higher immersion times of about 5 minutes in the solution of 0.5% HF in water, permitted the eutectic phase to be examined in detail, as can be seen in Fig. 5(b). Typical optical and SEM micrographs with the measured secondary dendritic arm spacings (λ_2) and interphase spacings (λ) are also shown. It can be seen that both λ and λ_2 increase with the increasing distance from the cooled bottom of the Al-3 wt.% Ni alloy casting.

Fig. 6 evidences the Al_3Ni intermetallic peaks, which were also detected in the XDR pattern of the as-cast Al-3 wt.% Ni alloy sample, similarly to those observed in the XDR patterns of atomized and hot-extruded powder samples, shown in Fig. 2.

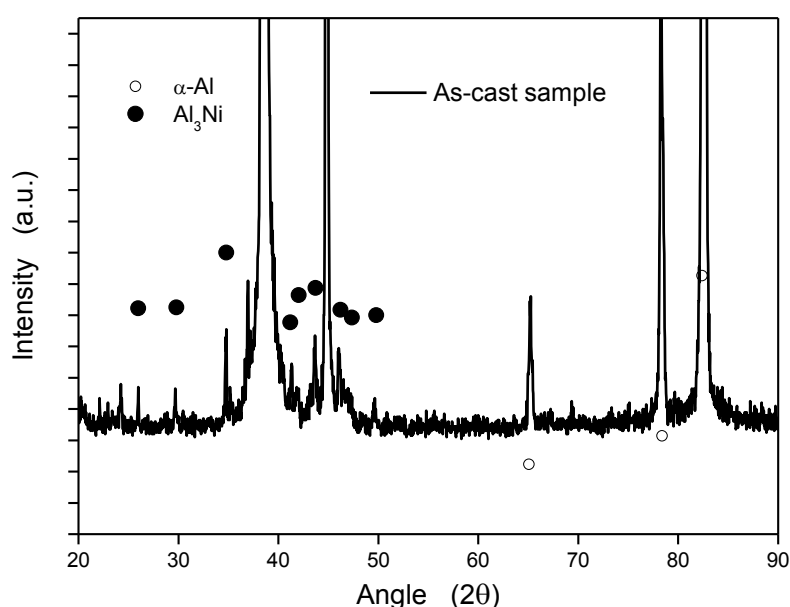
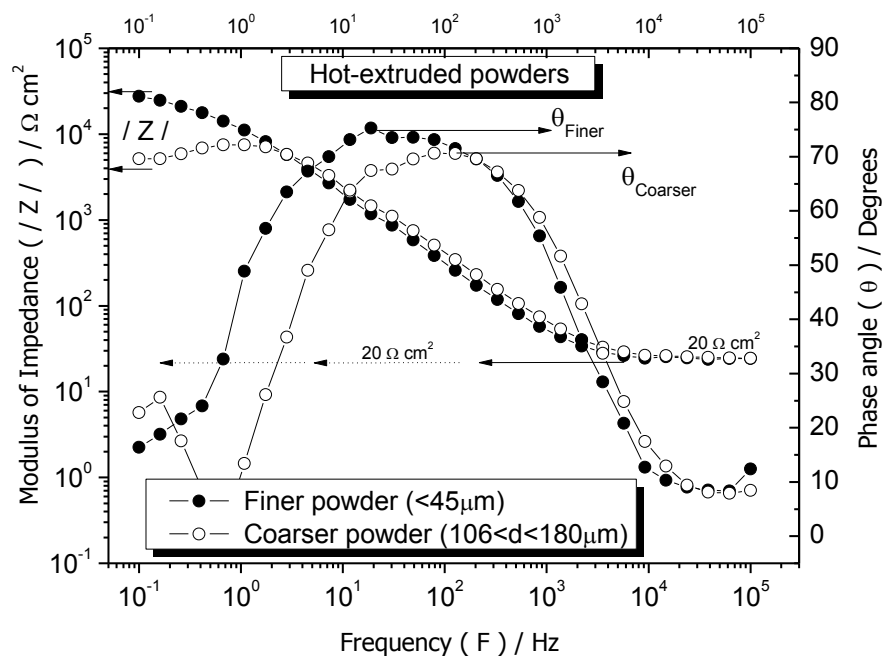


Figure 6. XRD patterns of the as-cast Al-3 wt.% Ni alloy sample.

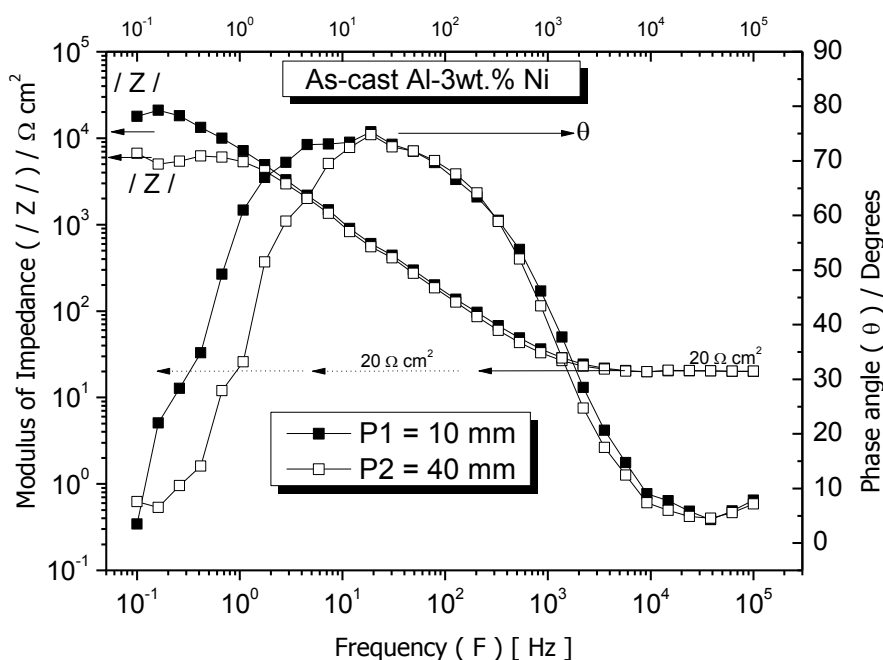
3.3. EIS and equivalent circuit measurements

Fig. 7 shows experimental Bode and Bode-phase plots for both the hot-extruded powders (HP) and as-cast (AC) Al-3 wt.% Ni alloy samples. Fig. 7 (a) depicts the experimental Bode plots with the modulus of impedance ($|Z|$) vs. frequency for hot-extruded powder samples, which are characterized by three distinct regions, i.e.: (i) at a frequency of 10^{-1} Hz, $|Z|$ attain values of about $27.2 \text{ k}\Omega \text{ cm}^{-2}$ and $5.2 \text{ k}\Omega \text{ cm}^{-2}$ for the finer and coarser hot-extruded powders, respectively, which correspond to the resistance of the sample; (ii) between frequencies of 4×10^3 and 10^5 Hz, $|Z|$ is about $20 \Omega \text{ cm}^{-2}$, indicating that the impedance is dominated by the electrolyte resistance (0.5 M sodium chloride solution); and finally (iii) in the broad low and middle frequency ranges (10^0 to 10^3 Hz and $5.8 \text{ k}\Omega \text{ cm}^{-2}$ to $20 \Omega \text{ cm}^{-2}$), linear slopes of about -1 are displayed, indicating a capacitive behavior. Considering the Bode-phase plots for the hot-extruded powder samples, the maximum phase angles

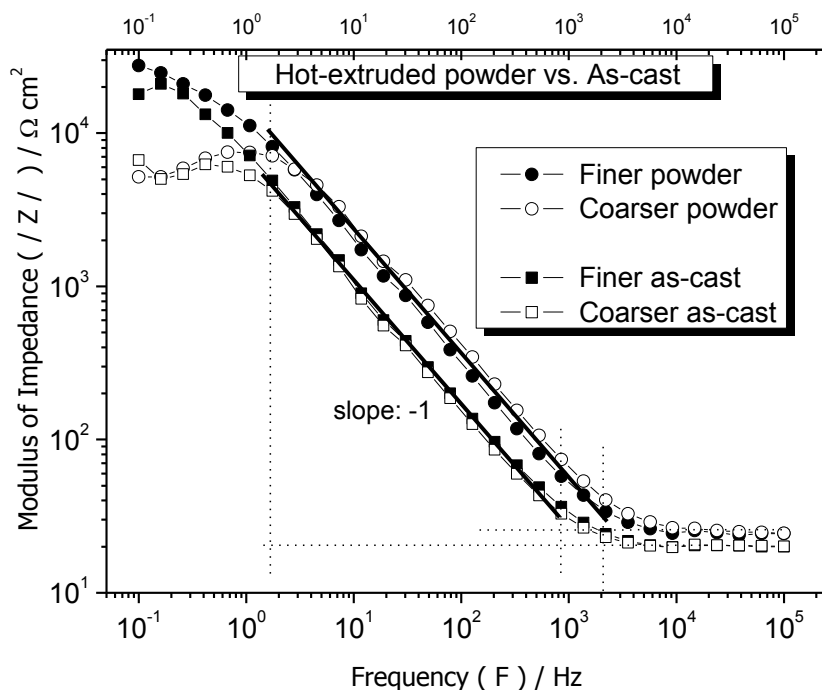
(θ_{max}) of the finer and coarser hot-extruded (HE) powder samples are 75° associated with $19 (\pm 1)$ Hz and $70 (\pm 1)$ degree with $80 (\pm 2)$ Hz, respectively. This slight displacement toward a lower phase angle and a higher frequency associated with the coarser hot-extruded powder sample indicates a deleterious effect on its corresponding electrochemical behavior. These Bode-phase plots depict the occurrence of similar double layer formation and two constant times, suggesting similar corrosion mechanisms, as shown in Fig. 7(a).



(a)



(b)



(c)

Figure 7. Experimental EIS plots for (a) hot-extruded (HE) Al-3 wt.% Ni alloy powders samples, (b) as-cast (AC) Al-3 wt.% Ni alloy samples, and (c) comparison of Bode plots for the HE and AC samples in a 0.5 M NaCl solution at 25 °C.

Fig. 7 (b) shows both Bode and Bode-phase plots for as-cast Al-3 wt.% Ni alloy samples at positions P1 = 10 mm and P2 = 40 mm from the bottom of the casting. Bode plots depicts $|Z|$ as a function of frequency characterizing three distinct regions: (i) at a low frequency (of 10^{-1} Hz) representing the resistance of the sample, $|Z|$ values are $16.9 \text{ k}\Omega \text{ cm}^{-2}$ and $6.7 \text{ k}\Omega \text{ cm}^{-2}$ for positions P1 and P2, respectively; (ii) between frequencies of 4×10^3 and 10^5 Hz, $|Z|$ is about $20 \Omega \text{ cm}^{-2}$, indicating that the impedance is dominated by the electrolyte resistance; and (iii) at frequencies between 10^0 to 10^3 Hz a linear slope of about -1 is displayed. The maximum phase angle (θ_{\max}) of both finer and coarser as-cast Al-Ni alloy samples are 73° associated with $18 (\pm 1)$ Hz.

Fig. 7(c) shows a comparison between the experimental Bode plots and two interesting aspects are evidenced: (i) the evolution of the capacitive double layer is very similar for both finer and coarser HE powder samples and are also very similar for the as-cast samples. However, considerably different -1 slopes with respect to frequency are observed, which is an evidence that different kinetics of double layer formation are associated with the samples obtained by the dissimilar metallurgical processes; (ii) both finer microstructures of HE and AC have similar $|Z|$ between 20 and $23 \text{ k}\Omega \text{ cm}^{-2}$, and similar $|Z|$ are also observed for both coarser microstructures of HE and AC samples (from 6 or $7 \text{ k}\Omega \text{ cm}^{-2}$).

Fig. 8 displays comparisons between the experimental Nyquist plots for both coarser and finer HE powder samples and finer and coarser AC samples corresponding to the Bode and Bode-phase plots shown in Fig. 7. It can be seen that the capacitive semi-arcs for all the samples examined have similar shapes, indicating similar kinetics of oxide film formation. It can also be said that both finer HE and AC samples have similar semi-arcs and both coarser HE and AC samples have also similar

capacitive semi-arcs. Both components Z_{Real} (in-phase) and the $Z_{Imaginary}$ (out-of-phase) evidence a considerable increase (of about 3 times) when the results of coarser HE powders and coarser as-cast Al-3 wt.% Ni alloy samples are compared. These observations give indications that for finer microstructure arrays, independently of the type of metallurgical processing chosen, i.e. casting or atomization followed by hot-extrusion, the resulting electrochemical behaviors are very similar, and better than those of coarser HE and AC samples.

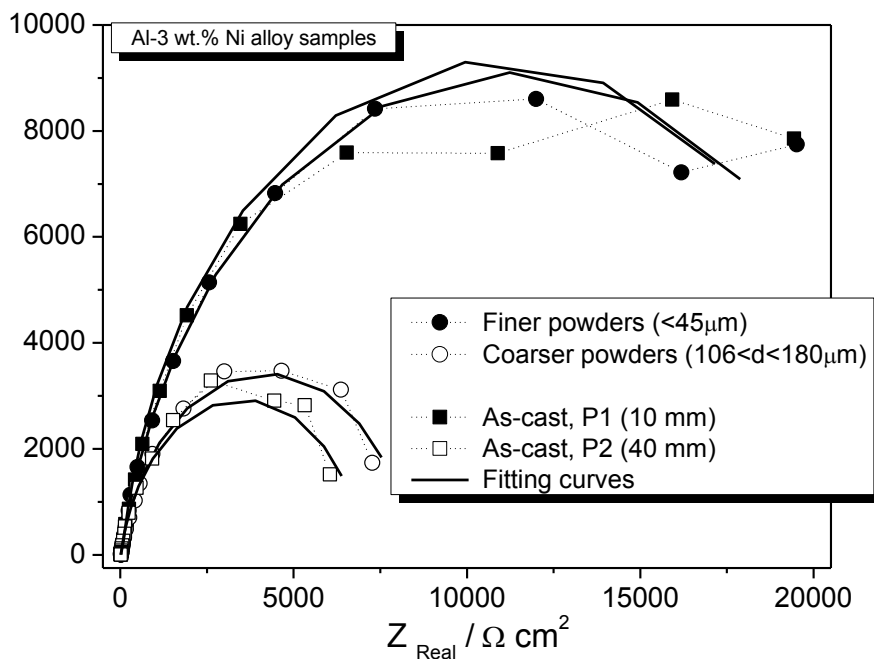


Figure 8. Experimental and simulated Nyquist plots of hot-extruded powders and as-cast Al-3 wt.% Ni alloy samples in a 0.5 M NaCl solution at 25 °C.

In order to give quantitative support to the experimental EIS results, impedance parameters were obtained by the ZView[®] software adopting a well-known complex equivalent $R_{el}(R_1(Z_{CPE(1)}(Z_{CPE(2)}R_2))$ circuit [8,10,16-22], as shown in Fig. 9. In the proposed equivalent circuit, R_{el} , R_1 and R_2 are the electrolyte resistance, the charge transfer resistance and stands for a polarization resistance due to the participation of adsorbed intermediates, respectively. For simplicity, a constant-phase element (CPE) representing a shift from an ideal capacitor was used instead of the capacitance itself.

The parameters $Z_{CPE(1)}$ and $Z_{CPE(2)}$ denote the double layer capacitance and the capacitance associated with the polarization resistance R_2 . The parameters n_1 and n_2 are correlated with the phase angle, varying between -1 and 1. $Z_{CPE} = [C(j\omega)^n]^{-1}$ denotes the impedance of a constant phase element [8, 10, 16-22], where C is the capacitance; j is the current; ω is the frequency and $-1 \leq n \leq 1$. The value of n can also be associated with the non-uniform distribution of current as a result of surface defects or roughness [8, 10, 16-22].

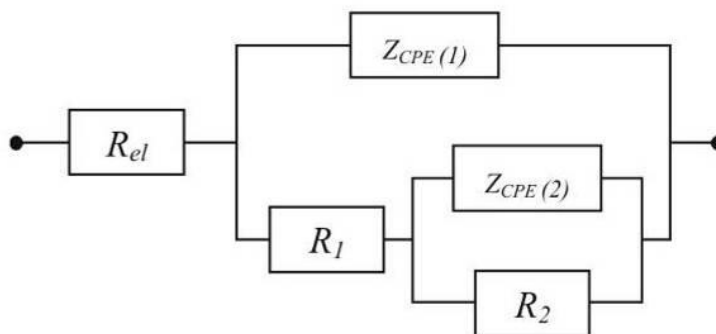


Figure 9. Proposed equivalent circuit used to obtain impedance parameters.

The impedance parameters obtained by the ZView[®] software, are shown in Table 1. Simulated and experimental curves are shown in Nyquist plots (Fig. 8). The fitting quality was also evaluated by using chi-squared (χ^2) values, which are about 61 to 98 $\times 10^{-4}$, as also shown in Table 1.

Comparing the impedance parameters of the two examined HE powder Al-Ni alloy samples, it can be seen similar $Z_{CPE(1)}$ and R_1 values for both finer and coarser samples, i.e. of about $1.5 \mu\text{Fcm}^{-2}$ and $5 \Omega \text{cm}^2$, respectively. On the other hand, the highest R_2 ($22.7 \text{ k}\Omega \text{cm}^2$) is associated with the finer HE sample, which is of about 3 times higher when compared with that of the coarser HE sample ($8.4 \text{ k}\Omega \text{cm}^2$). Considering the impedance parameters of the as-cast Al-Ni alloy samples, it can also be seen similar $Z_{CPE(1)}$ and R_1 values ($14 \mu\text{Fcm}^{-2}$ and $485 \Omega \text{cm}^2$). Although the coarser as-cast sample ($P = 40 \text{ mm}$; $\lambda_2 = 18 \mu\text{m}$) has a capacitance $Z_{CPE(2)}$ (of about $6 \mu\text{Fcm}^{-2}$) which is similar to that of the finer AC sample, its corresponding R_2 is of about 3 times lower (about $21 \text{ k}\Omega \text{cm}^2$ and $7 \text{ k}\Omega \text{cm}^2$, respectively). It is well-known that R_1 and R_2 are the polarization resistances of the porous and barrier layers, respectively. In Table 1, it is evidenced that R_2 is significantly higher than R_1 (porous layers), which indicates that the protection seems predominantly provided by R_2 .

Comparing the impedance parameters of the HE and AC samples, it is clearly observed that both R_1 and $Z_{CPE(1)}$ are of about 10 times higher for the AC samples. Since R_1 stands for the charge transfer resistance and $Z_{CPE(1)}$ for the double layer capacitance corresponding with an outer porous layer, it can be said that the HE samples has a faster double layer formation than the AC powder samples, which can be observed by the slopes of Fig.7(c). It is known that the capacitance decreases as the oxide (or intermediate product) layer thickness is increased, which can also decrease the film dielectric constant [23-24]. On the other hand, it is expected a significant increase in the inner (barrier) layer thickness due to the reactions between metastable oxides (or intermediates), located in the outer porous layer, and the electrolyte. With this, due to electrochemical affinities some less stable oxides (or intermediates) are transformed in more stable oxide particles, which are incorporated into the inner layer. From the metallurgical point of view, it seems that the finer microstructures (of both the HE powders and AC samples) induce faster reactions that lead to an increase in the thickness of the inner barrier layer, and this is intimately associated with the R_2 values shown in Table 1. In this context, with these observations, there are indications that a better electrochemical behavior is connected to samples having finer microstructures. However, it still unclear why the coarser AC and HE samples show similar impedance parameters, as well as the finer microstructures of both AC and HE samples, as

shown in Figs. 7 and 8. It seems that the cathode/anode area ratio (considering the microstructural arrangement of the Al-rich matrix; anode and the Al₃Ni intermetallic particles; cathode) has a significant role that could explain the observed electrochemical behavior.

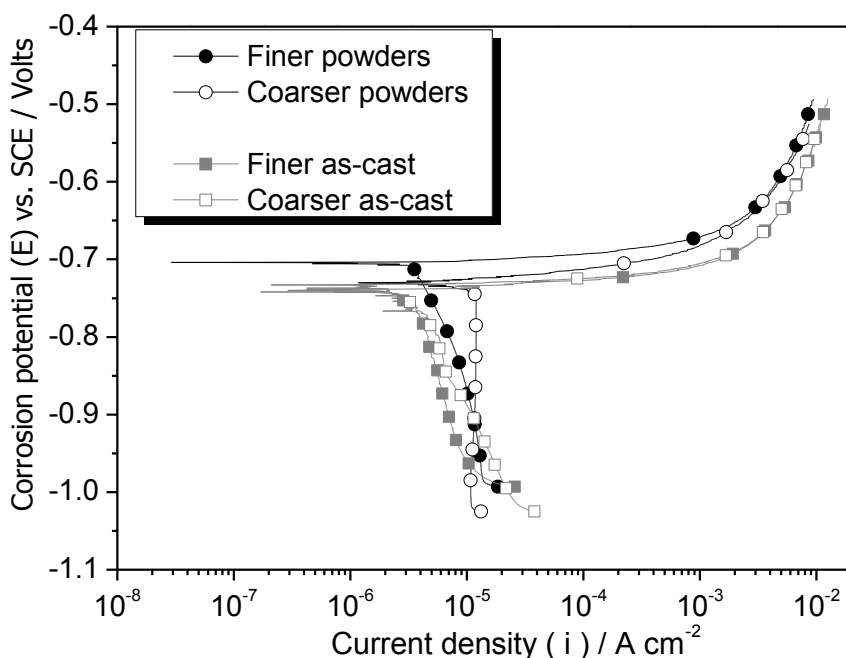
However, it would also be important to provide a comparison between the experimental results of the potentiodynamic polarization curves of these alloys samples in order to better understand their corresponding electrochemical behavior.

3.4. Potentiodynamic polarization measurements

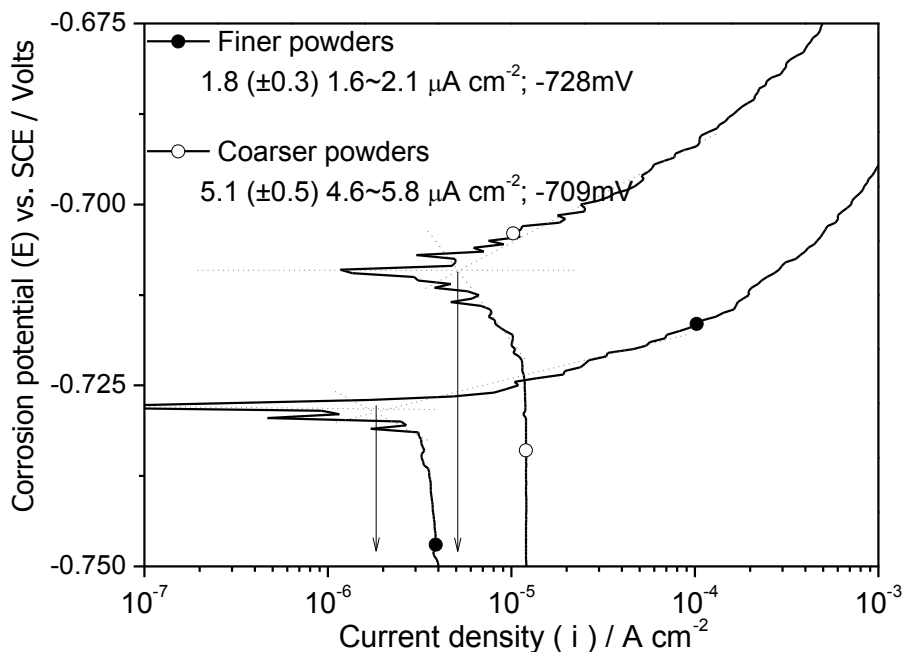
Comparisons of experimental potentiodynamic polarization curves in a 0.5 M NaCl solution at room temperature of HE powder and AC Al-3 wt.% Ni alloy samples are accomplished in Fig. 10. Experimental potentiodynamic polarization curves of samples between -1.02 V to -0.5 V (SCE) are shown in Fig. 10(a). In order to show details of these curves Fig. 10(b) and 10(c) highlight the results between -750 mV and -675 mV (SCE) and between -760 mV and -720 mV (SCE) for the HE powder and AC samples, respectively.

Considering Fig. 10 (a), it can be said that the all samples examined have anodic and cathodic branches of similar shapes and spikes are also evidenced, which can be associated with pitting and repassivation, as previously reported [8-10].

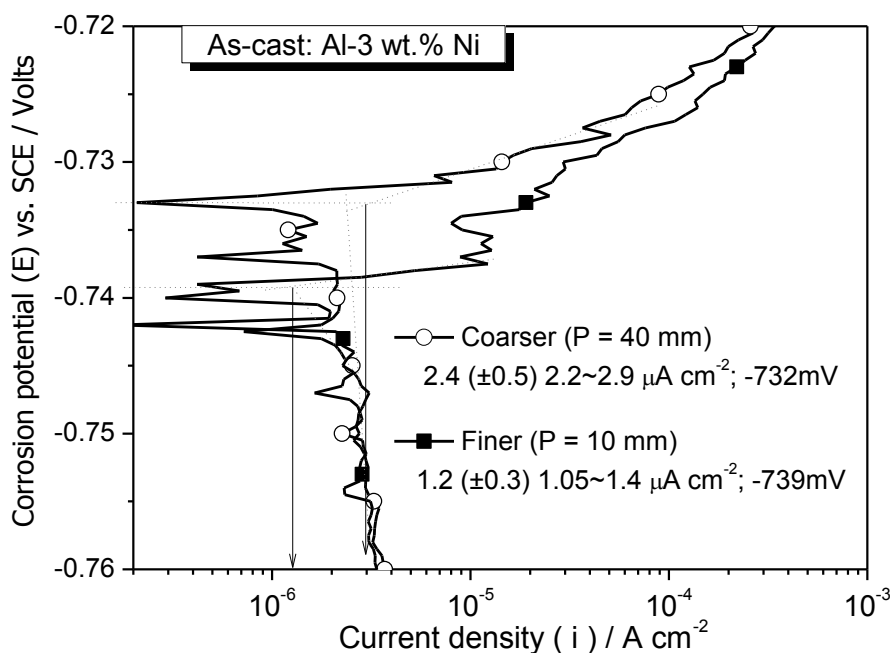
Although the coarser HE powder sample has its corrosion potential (-709 mV, SCE) slightly displaced toward the nobler-side potential (of about 20 mV, SCE) when compared with the finer HE sample, its corresponding current density ($\pm 5 \mu\text{A cm}^{-2}$) increased of about three times when compared with that of the finer HE powder sample ($\pm 1.8 \mu\text{A cm}^{-2}$ and -728 mV, SCE), as shown in Fig. 10 (b). Considering Tafel's extrapolation [23-24], the extrapolated lines evidenced even higher current densities for the coarser HE powder sample.



(a)



(b)



(c)

Figure 10. (a) Experimental anodic/cathodic potentiodynamic polarization curves of both HE and AC alloy samples, (b) detailed results for the hot-extruded (HE) powders samples and (c) detailed results for the as-cast (AC) Al-3 wt.% Ni alloy samples in a 0.5 M NaCl solution at 25 °C.

Fig. 10(c) evidences a current density of $2.4 (\pm 0.5) \mu\text{A cm}^{-2}$ associated with -732 mV (SCE) for the coarser as-cast (AC) Al-Ni sample while the finer AC sample has a current density of $1.2 (\pm 0.3) \mu\text{A cm}^{-2}$ with a corrosion potential of -739 mV (SCE) , which again suggests that a finer dendritic

matrix and finely and more homogeneously distributed Al₃Ni intermetallic particles can be associated with a better electrochemical corrosion resistance.

Comparing all the examined polarization curves, it can be observed that both cathodic and anodic branches evidenced oscillations which can be associated with pitting mechanisms. It is also clearly observed that the as-cast (AC) samples have lower current densities than those of the hot-extruded (HE) powder samples.

3.5 Correlation between microstructure and electrochemical parameters

3.5.1 Effect of alloy Ni content

The present results for the Al-3 wt.% Ni alloy depict an opposite trend with respect to the electrochemical corrosion behavior when compared with that previously reported for an Al-5 wt.% Ni alloy [8-9]. In the latter case it was shown that finer microstructures were associated with worse general corrosion resistance and better pitting corrosion when compared with a coarser microstructure. From the metallurgical point of view, it is important to point out that a solute Ni content of 5 wt.% is much closer to the eutectic composition (6.1 wt.%Ni) than the alloy currently examined (Al-3 wt.% Ni alloy). At the eutectic temperature (642 °C), the equilibrium partition coefficient (k) can be calculated as $k = C_S / C_L = 0.05/6.1 = 0.008$, where C_S and C_L are the solid and liquid compositions (solubility limit and eutectic compositions, respectively). This parameter (k) can be used into Scheil's equation [25] to estimate the eutectic fraction (f_E) formed during non-equilibrium solidification of each alloy: Al-5 wt.% Ni alloy ($f_E = \pm 82\%$) and Al-3 wt.% Ni alloy ($f_E = \pm 49\%$)[8]. Besides, it should also be considered that the upward vertical directional solidification in water-cooled chill molds induces positive macrosegregation at regions which are closer to the cooled bottom of the casting for both Al-5 and 3 wt.% Ni alloys [8], where the corresponding eutectic fractions can attain values of about 95% [8] and 62%, respectively.

Due to the higher Ni content, and consequently a higher eutectic fraction, the resulting microstructure of the Al-5 wt.% Ni alloy is considerably finer than that of the Al-3 wt.% Ni alloy considering the entire casting length, as previously reported [26]. This permits to consider that the Al₃Ni intermetallic particles in the interdendritic regions are more homogeneously distributed and more interconnected for the Al-5 wt.% Ni alloy when compared with similar regions of the Al-3 wt.% Ni alloy microstructure. Besides, it was also previously observed that the Al-3 wt.% Ni alloy solidified at a higher cooling rate (about 4.5 °C/s at 17 mm from the surface casting) and growth rate (0.8 mm/s at the same position) [7] than the Al-5 wt.% Ni alloy (about 1.5 °C/s and 0.35 mm/s) [7-8], which also favors the formation of a non-interconnected network of Al₃Ni intermetallic particles, independently if fiber-like or globular-like Al₃Ni particles are formed, as previously reported [7-9].

Additionally, it has also been reported by Belov et al. [1] that high cooling rates tend to provide both fragmentation and globularization effects on the Al₃Ni intermetallic particles, which reinforces the indications that the Al-3 wt.% Ni alloy tends to be constituted by more non-interconnected globular-like Al₃Ni particles than the Al-5 wt.% Ni alloy. Due to both the eutectic fraction and morphology of Al₃Ni particles, the cathode/anode area ratios of the Al-3 wt.% Ni and Al-5 wt.% Ni

alloys are considerably different. This will induce a faster dissolution of the Al-rich matrix of the Al-5 wt.% Ni alloy.

3.5.2 - Effect of morphology and cathode/anode area

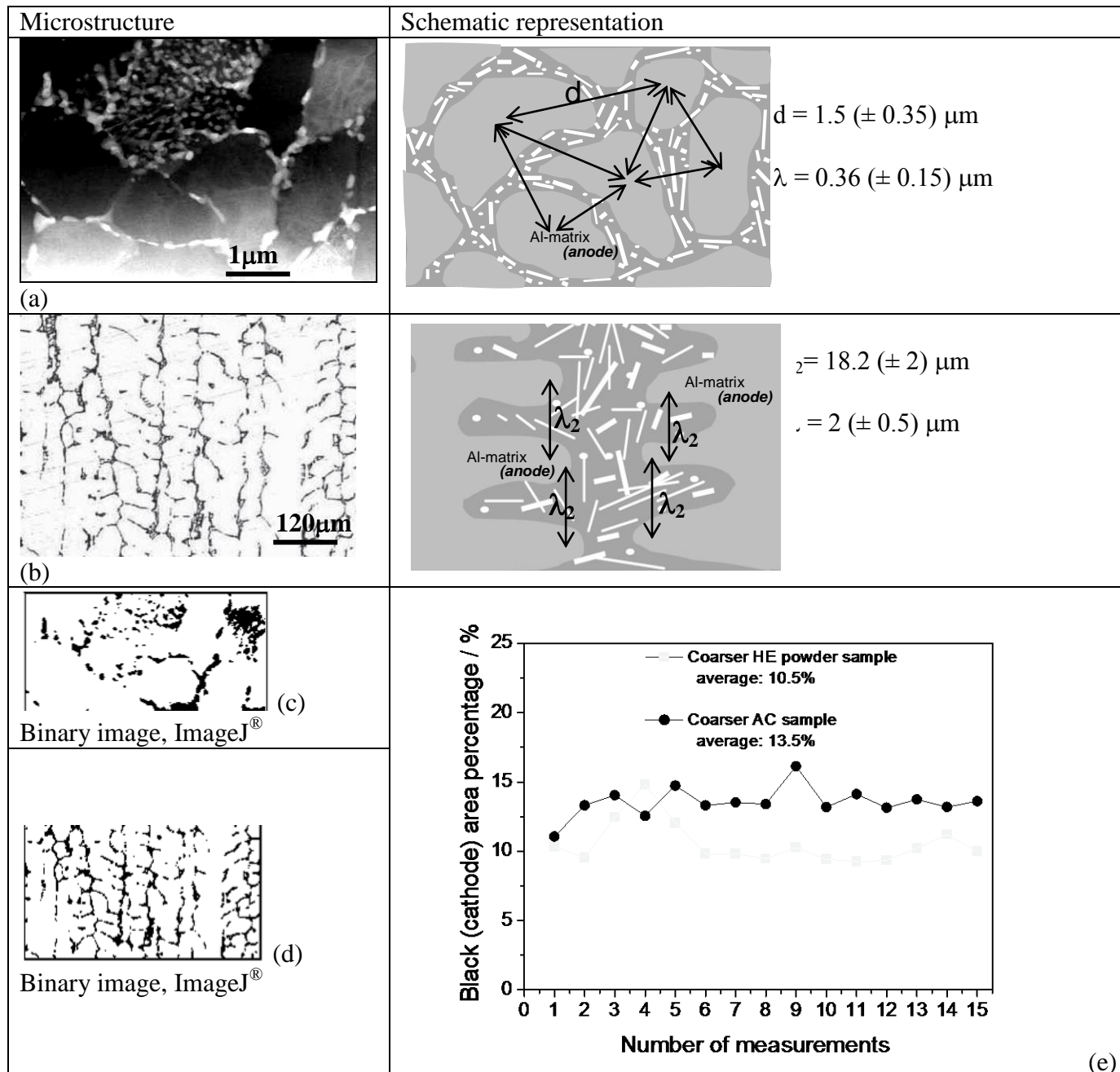


Figure 11. Microstructure and schematic representation of the coarser microstructural morphology of (a) the HE powder sample; (b) AC sample evidencing the microstructural parameters, (c) and (d) binary image from ImageJ[®] and (e) cathode area percentage (eutectic mixture: Al-phase + Al₃Ni particles).

Fig. 11 depicts the typical resulting coarser microstructures and their corresponding schematic representations of the Al-rich matrices (in both cellular and dendritic arrays) and Al₃Ni intermetallic particles (HE powder and AC Al-3 wt.% Ni alloy samples). Considering the microstructural parameters of the coarser HE powder sample, it can be said that the distance between the centers of adjacent Al-rich matrix cells (d) is about $1.5 \pm 0.35 \mu\text{m}$ associated with an interphase spacing of about $0.36 \pm 0.15 \mu\text{m}$, i.e. a " d/λ " ratio of about 4. Similar analysis made with the coarser AC samples reveals that the representative distance between the centers of adjacent dendritic branches of the Al-rich matrix, i.e. the secondary dendrite arm spacing (λ_2) is about $18.2 \pm 2 \mu\text{m}$ associated with an interphase spacing of $2 \pm 0.5 \mu\text{m}$, i.e. a " λ_2/λ " ratio of about 10. It is also important to remark that the light gray areas represent the Al-rich matrix, which in equilibrium solidification conditions attains a concentration of about 0.03 wt. Ni (according to Scheil's Equation, $C_S = k C_0$). The dark gray is the eutectic mixture constituted by: Al-rich phase (about 0.05 wt. % Ni) and Al₃Ni (~40 wt.% Ni) intermetallics (white particles).

Typical binary images from the microstructures of both HE and AC samples obtained by the ImageJ[®] software are shown in Fig. 11(c) and (d), respectively. From these binary images the black area percentage (cathode), representing the mixture of Al-phase + Al₃Ni particles was determined. The complementary area represents the anode white regions (Al-rich matrix: cellular or dendritic). Although the ratios of the representative Al-rich matrix distance and interphase spacings of the examined coarser HE and Ac samples are significantly different, the binary images indicate similar cathode/anode area ratios ($A_{c/a}$) for both samples, i.e. of about 10.5% and 13.5%, respectively.

Despite the similar cathode/anode area ratios ($A_{c/a}$) of both coarser microstructures of the HE powder and AC alloy samples, this ratio $A_{c/a}$ can change considerably with the evolution of corrosion. This change is intimately associated with the morphology of the Al₃Ni intermetallics of the eutectic mixture. A rapidly solidified sample (high cooling rate) has a fine microstructure array with a network of globular and/or fragmented Al₃Ni intermetallic particles, as previously reported by Belov et al. [1], and also shown in Figs. 3(c) and (d) and Fig.4.

Fig. 12 suggests that the two distinct cathode/anode areas are formed: (i) eutectic mixture (Al-rich phase in the interdendritic region + Al₃Ni particles) and Al-rich matrix, and (ii) eutectic mixture of Al₃Ni particles and Al-rich phase. With the evolution of corrosion, the ratio " $A_{c/a}$ " changes progressively. Under low cooling rate conditions during solidification, an interconnected Al₃Ni intermetallic network is expected. The " $A_{c/a}$ " ratio is modified along corrosion action and the cathode area constituted by fiber-like Al₃Ni particles increases since the Al-rich phase (in the eutectic mixture) is corroded. With this increase in the cathode area, the Al-rich phase is intensively and progressively corroded, as schematically shown in Fig. 12(b). Obviously the Al-rich matrix is also corroded with respect to the cathode eutectic mixture, as shown in Fig. 12(a). On the other hand, when fragmented and/or globular Al₃Ni intermetallic particles are formed (high cooling rates during solidification), the " $A_{c/a}$ " ratio is also considerably modified, however, the cathode area decreases more rapidly since the globular or fragmented Al₃Ni particles are detached from the eutectic lattice. In this sense, the anode area increases and the corrosion process tends to stabilize due to Al-oxide film formation (or corrosion-by-product formation) on the surface sample, as schematically depicted in Fig. 12(c). A

more homogeneously and finely distribution of Al_3Ni particles in the Al-rich lattice will provide a decrease in corrosion action due to an “enveloping effect” provided by anode and cathode areas.

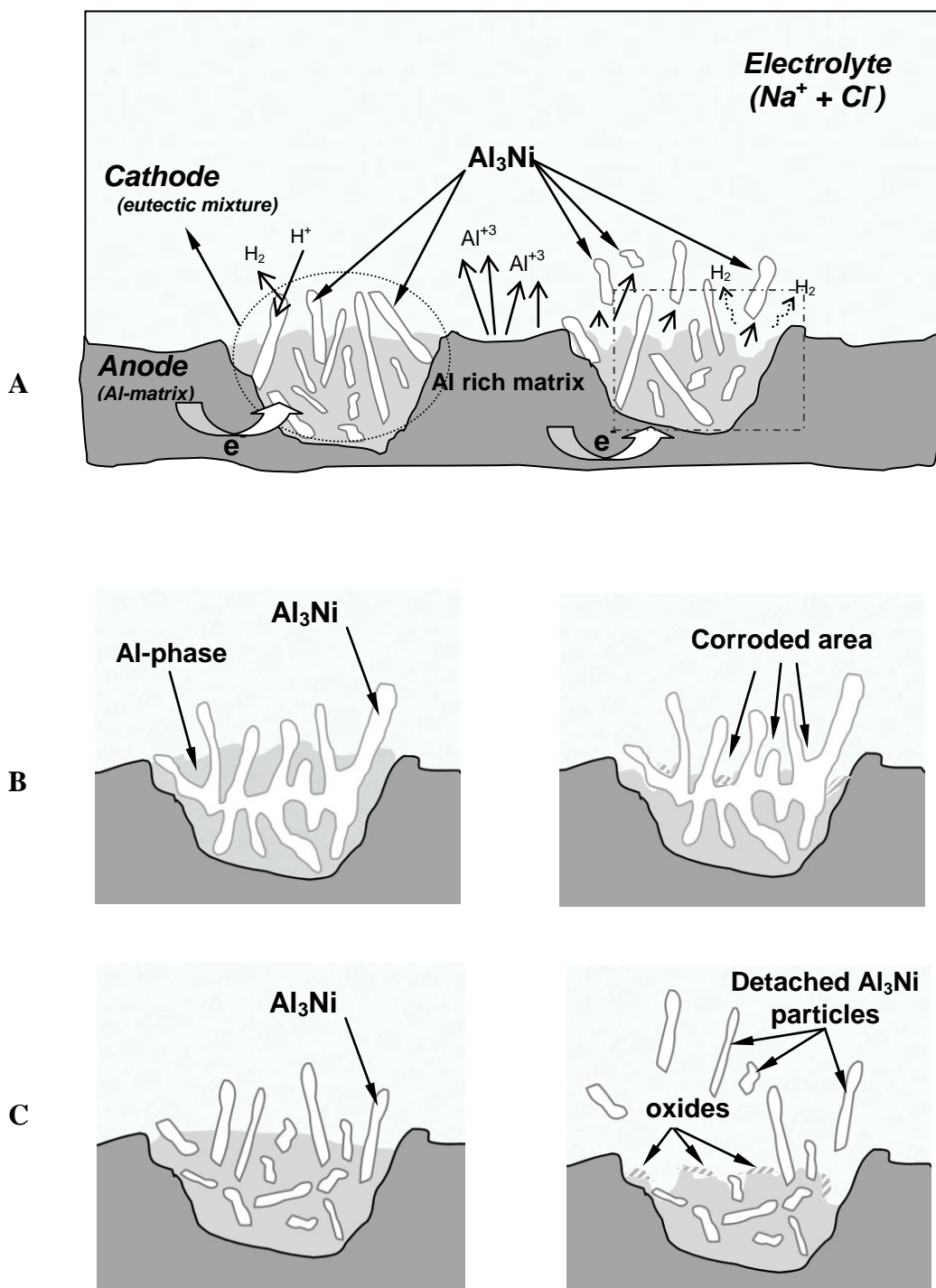


Figure 12. Typical representation of: (a) the two distinct cathode/anode areas constituted by (i) eutectic mixture and Al-rich matrix, and (ii) Al_3Ni particles and Al-rich phase (eutectic mixture), (b) corrosion when Al_3Ni particles are interconnected and (c) corrosion when Al_3Ni particles are non-interconnected.

Based on the experimental results of the potentiodynamic polarization curves (oscillations in both anodic and cathodic branches), it seems that a galvanic effect between the Al₃Ni intermetallics and the Al-rich phase should be considered. Al₃Ni has a cathode role with oxygen and/or hydrogen reduction, which seems to accelerate the dissolution of the Al-rich phase surrounding the Al₃Ni particles induced by Al³⁺ ions provided by the reaction $Al \rightarrow Al^{3+} + 3e^-$.

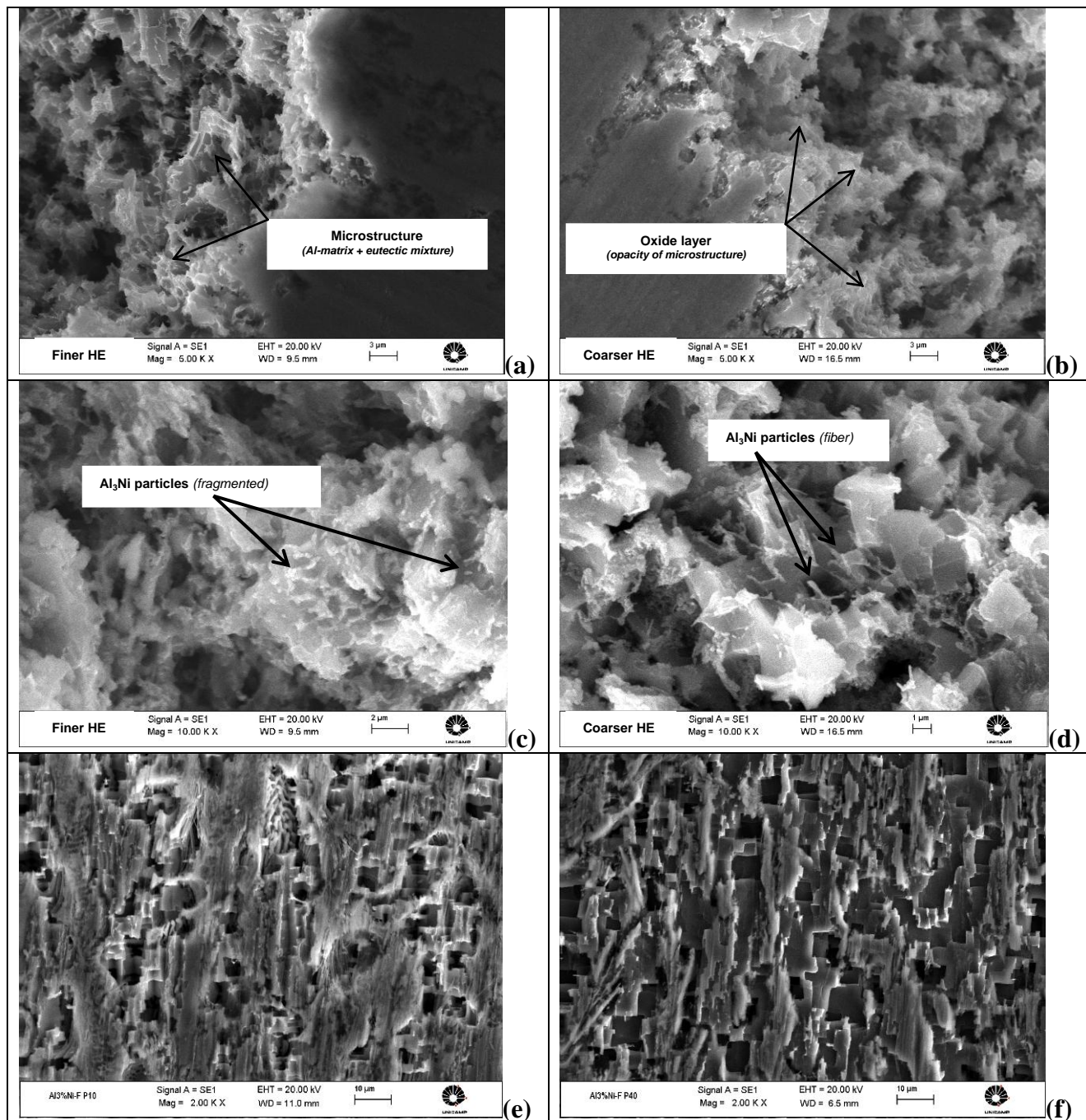


Figure 13. Typical corroded images of the hot-extruded (HE) powder Al-3 wt.% Ni alloy samples after EIS and polarization tests evidencing (a) and (c) finer microstructures and (b) and (d) coarser microstructures; and typical corroded images of the as-cast (AC) Al-3 wt.% Ni alloy samples with (e) finer and (f) coarser microstructure arrays.

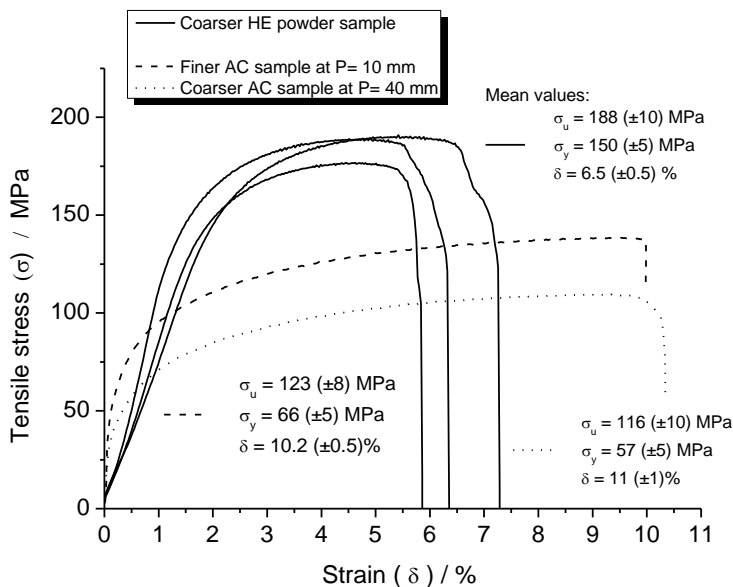
Fig. 13 shows post-mortem images of the coarser and finer microstructures of both the HE powders and the as-cast (AC) samples after EIS and polarization tests. Figs. 13(a) and (b) indicate that intensive oxide layer formation occurred on the surface of the coarser HE sample, which can be identified by an opaque layer, as shown in Fig. 13(b). On the other hand, the resulting microstructure constituted by the Al-rich matrix and eutectic (white regions) is clearly observed in Fig. 13 (a).

Comparison between Fig. 13(c) and (d) also evidences that fiber-like Al_3Ni particles tend to be formed in the HE coarser microstructure sample, while the finer HE powder sample has fragmented and/or globular intermetallic particles. Fig. 13 (e) and (f) shows the typical SEM images after EIS and polarization tests of both finer and coarser as-cast (AC) Al-3 wt.% Ni alloy samples in a 0.5 M NaCl solution at room temperature. Again it can be seen that coarser microstructure arrays were more intensively corroded when compared with samples having finer microstructures. These observations give support to the previous discussions concerning the experimental and simulated results of EIS and polarization tests.

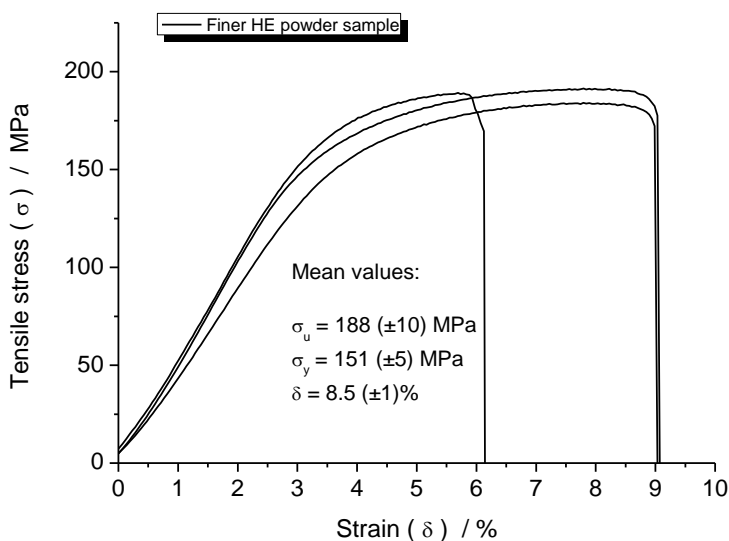
3.6 Corrosion behavior vs. tensile mechanical properties

It is well known that the improvement of a property without provoking deleterious effects in another property is a great challenge in engineering applications. In this context, the mechanical behavior of the hot-extruded powder and as-cast samples will be investigated by monotonic tensile tests. The goal is to provide a combined plot of ultimate tensile strength (UTS) and current density (i) for all the examined Al-3 wt.% Ni alloy samples. The aim of such combined plot is to design an “ideal” range of microstructural array which determines a region with a compromise between good electrochemical corrosion behavior and good tensile strength.

Fig. 14 (a) and (b) shows the behavior of both HE powder and AC samples under tensile tests. It can be seen that the material extruded from the initial powder sizes less than $45\ \mu\text{m}$ (finer microstructure) presented a yield stress (σ_y) of about 151 ± 5 MPa, an ultimate tensile stress (σ_u) of 188 ± 10 MPa and an elongation (δ) of about 8.5 %. Except for the difference in the elongation (δ) of about +2% associated with the finer HE sample, similar results of both σ_y and σ_u are observed for the coarser HE powder sample, i.e. of about 150 ± 5 MPa and 188 ± 10 MPa, respectively. These results show that the route adopted for the hot consolidation process of the nanostructured Al-3 wt.% Ni alloy was very effective for the entire range of powder sizes and promoted yield and ultimate stress of approximately 2.3 times and 1.5 times higher, respectively, when compared with the corresponding results obtained for the as-cast (AC) Al-3 wt.% Ni alloy samples, as can be seen in Fig. 14(a). These results indicate that for the examined Al-3 wt.% Ni powder alloy and the parameters of consolidation adopted, the differences in powder size have not significantly affected the resulting mechanical properties. Considering the as-cast (AC) samples, as expected, the results have shown that the samples having finer microstructure arrays provided better mechanical behavior when compared with those having coarser arrays.



(a)



(b)

Figure 14. Engineering stress-strain diagrams: (a) hot-extruded Al-3 wt.% Ni alloy with powder sizes between 180-106 μm (coarser HE powder) and as-cast (AC) Al-3 wt.% Ni alloy samples at positions (a) 10 and 40 mm; (b) hot-extruded Al-3 wt.% Ni alloy with powder sizes lower than 45 μm (finer HE powder).

Fig. 15 combines electrochemical corrosion behavior expressed by the corrosion current density (i) and ultimate tensile strength (σ_u), both plotted as a function of a microstructure parameter for all examined Al-3 wt.% Ni alloy samples, i.e. the parameters “d” and “ λ_2 ” for the hot-extruded (HE) powder samples and as-cast (AC) samples, respectively. These “d” and “ λ_2 ” parameters characterize the distribution of the Al-rich matrix throughout the microstructure. It is important to remember that the ratios of these parameters with the interphase spacing, λ , (i.e. “d/ λ ” and “ λ_2/λ ”) are

quite different, although the cathode/anode microstructural area ratio for the HE and AC samples are very similar, as aforementioned.

It can be concluded that there exists an important role of the resulting microstructure on both mechanical and electrochemical behavior of the HE and AC Al-Ni alloy samples. Considering a determined range of microstructure parameter in Fig.15a, it can be observed that the current density proportionally increases with the decrease in the microstructure parameters (“d” or “λ₂”). For instance, considering a fine microstructural range between 0.45 and 1.5 μm, the current density increases about 3 times (from 1.8 to 5.1 μAcm²), which is directly proportional to the increase in the microstructural parameter. On the other hand, when the microstructure parameter increased about 2 times between range 9 and 18 μm, the current density has also experienced a similar proportional increase (from 1.2 to 2.4 μAcm²).

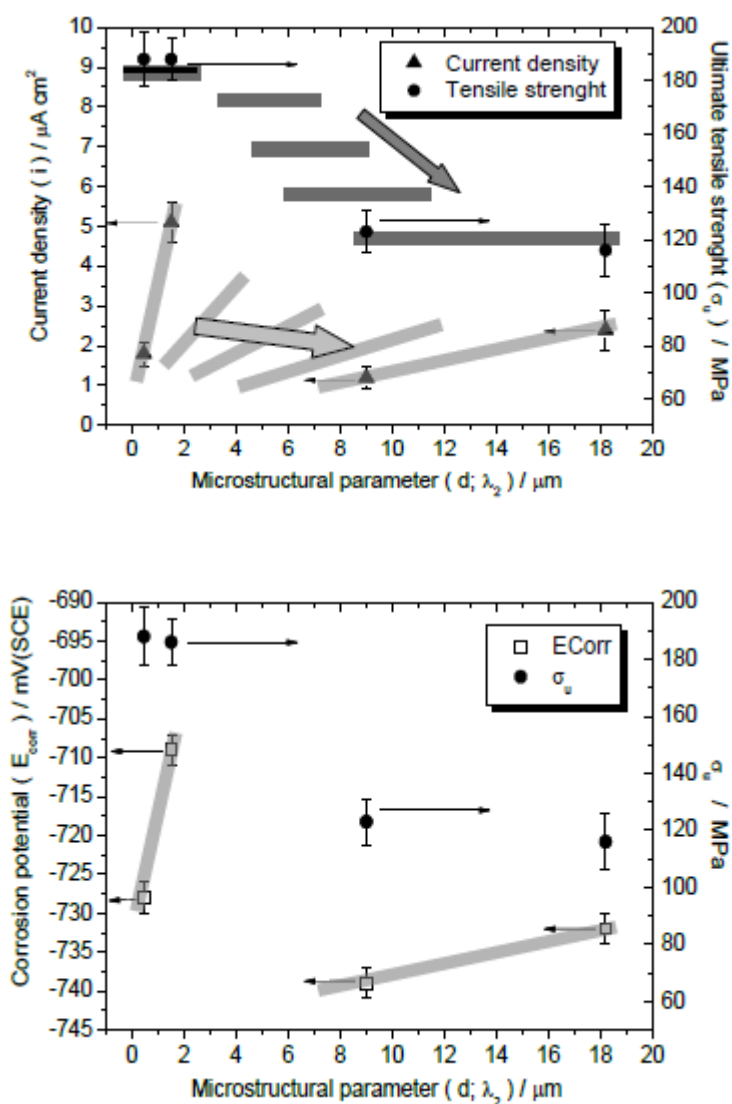


Figure 15. (a) Current density/ultimate tensile strength and (b) corrosion potential/ultimate tensile strength as a function of microstructural parameters (d or λ₂) for both HE powder and AC Al-3 wt.% Ni alloy samples.

It can also be concluded that there exists a plateau characterizing the correlation between mechanical properties and microstructure arrays. This plateau decreases with the increase in the range of microstructure parameter, as also shown in Fig. 15. These combined plots permit an “ideal” range of microstructural parameters to be designed, which determines a region with a compromise between good corrosion resistance and tensile strength.

4. CONCLUSIONS

From the present experimental investigation, the following conclusions can be drawn:

1) The hot-extrusion of Al-3 wt.% Ni alloy powders demonstrated that the intermetallic Al₃Ni particles are homogeneously distributed in the hot-extruded (HE) powder sample, which included an effective intragranular precipitation. A high resolution transmission electron micrograph (HRTEM) revealed Al- α grains and nanoprecipitate Al₃Ni intermetallic of about 3 nm at the grain boundaries.

2) The experimental results of EIS plots, impedance parameters obtained from the proposed equivalent circuit and potentiodynamic polarization curves indicated that finer microstructures (both hot-extruded and as-cast samples) have better electrochemical corrosion resistance than coarser ones.

3) Although distinct ratios between the representative distance of the Al-rich matrix and the interphase spacing have been determined, similar cathode/anode area ratios ($A_{c/a}$) for coarser microstructure arrays and finer microstructure arrays have been attained, independently of the applied method of production, i.e. hot-extrusion or unidirectional casting.

4) It was clearly evidenced a trend to obtain fragmented and/or globular Al₃Ni intermetallic particles with high cooling rates during solidification. With the progress of corrosion, these fragmented and/or globular Al₃Ni intermetallics are detached from the eutectic lattice, thus changing significantly the “ $A_{c/a}$ ” ratio, which can decrease considerably. The anode area increases and the corrosion process tends to stabilize due to Al-oxide film formation and by galvanic protection due to the enveloping effect between anode/cathode.

5) Considering the experimental results of mechanical properties, similar results have been determined for both ultimate tensile and yield strengths for coarser and finer hot-extruded powder samples, i.e. about 188 MPa and 150 MPa, respectively. The route adopted for the hot consolidation process of the nanostructured Al-3 wt.% Ni alloy was shown to be effective for the entire range of powder sizes, inducing yield and ultimate stresses of about 2.3 times and 1.5 times higher, respectively, when compared with the corresponding results obtained for the as-cast (AC) samples.

6) A synthesis of the present results combining electrochemical corrosion behavior and mechanical properties revealed that the resulting microstructure array has an important role on both properties. A combined plot of current density, corrosion potential and ultimate tensile strength as a function of a microstructural parameter permits the determination of a region with a compromise between good corrosion and mechanical resistances.

ACKNOWLEDGEMENTS

The authors acknowledge the financial support provided by FAEPEX-UNICAMP, CNPq (The Brazilian Research Council) and FAPESP (The Scientific Research Foundation of the State of São Paulo, Brazil).

References

1. N.A. Belov, A.N. Alabin, D.G. Eskin, *Scripta Mater* 50 (2004) 89.
2. B. Silva, I. Araujo, W. Silva, P.R. Goulart, A. Garcia, J.E. Spinelli, *Phil Mag Let* 91 (2011) 337.
3. W.H. Hunt Jr, *Powder Metall.*36 (2000) 51.
4. F.L. Catto, T. Yonamine, C.S. Kiminami, C.R.M. Afonso, W.J. Botta, C. Bolfarini, *J. Alloys Compd.* 509 (2011) S148.
5. E.J. Lavernia, J. Baram, E. Gutierrez, *Mater Sci. Eng.* 132A (1991) 119.
6. C.R.M. Afonso, J.E. Spinelli, C. Bolfarini, W.J. Botta, C.S. Kiminami, A. Garcia, *Mater. Res, in press.* <http://dx.doi.org/10.1590/S1516-14392012005000044>
7. M.V. Cante, J.E. Spinelli, N. Cheung, A. Garcia, *Metals Mater. Inter.* 16 (2010) 39.
8. W.R. Osório, L.C. Peixoto, M.V. Canté, A. Garcia, *Electrochim. Acta* 55 (2010) 4078.
9. W.R. Osório, L.C. Peixoto, M.V. Canté, A. Garcia, *Mater. Des.* 31 (2010) 4485.
10. W.R. Osório, J.E. Spinelli, C.R.M. Afonso, L. C. Peixoto, A. Garcia, *Electrochim. Acta* 69 (2012) 371.
11. P.A. Sivtsova, E. Yu, Neumerzhitskaya, V.G. Shepelevich, *Russian Metallurgy (Metally)*, 4 (2007) 327
12. K. Wada, S. Meguro, H. Sakamoto, *IEEE Transactions on Applied Superconductivity* 10 (2000) 1012.
13. J.Y. Uan, L.H. Chen, T.S. Lui, *Acta Mater.* 49 (2001) 313.
14. S.J. Hong, B.S. Chu, *Mater. Sci. Eng.* A348 (2003) 262.
15. A.M. Jorge Jr, M.M. Peres, J.B. Fogagnolo, C.S. Kiminami, C. Bolfarini, W.J. Botta, *Metall. Mater. Trans.* 40A (2009) 3314.
16. W.R. Osório, L.C. Peixoto, A. Garcia, *J. Power Sources*, 195 (2010) 1726
17. W.R. Osório, J.E. Spinelli, C.R.M. Afonso, L.C. Peixoto, A. Garcia, *Electrochim. Acta* 56 (2011) 8891
18. W.R. Osório, D.M. Rosa, A. Garcia, *Electrochim. Acta* 56 (2011) 8457
19. W.R. Osório, D.J. Moutinho, L.C. Peixoto, I.L. Ferreira, A. Garcia, *Electrochim. Acta* 56 (2011) 8412
20. W.R. Osório, D.M. Rosa, A. Garcia, *J. Power Sources* 175 (2008) 595.
21. W.R. Osório, C. Brito, L.C. Peixoto, A. Garcia, *Electrochim. Acta* 76 (2012) 218.
22. W.R. Osório, P.R. Goulart, A. Garcia, *Mater. Lett.* 62 (2008) 365.
23. M.A. Elmorsi, E. M. Mabrouk, R.M. Issa, M.M. Ghoneim, *Surf. Coat. Technol.* 30 (1987) 277.
24. Z. Shi, M. Liu, A. Atrens, *Corr. Scie.* 52 (2010) 579
25. W. Kurz, D.J. Fisher, *Fundamentals of Solidification*, *Trans. Tech. Public*, Switzerland, 1992.
26. M.V. Canté, J.E. Spinelli, I.L Ferreira, N. Cheung, A. Garcia, *Metall. Mater. Trans.* 39A (2008) 1712-1726